Piezoelectric Catalysis

International Edition: DOI: 10.1002/anie.201706549
German Edition: DOI: 10.1002/ange.201706549

Macroscopic Polarization Enhancement Promoting Photo- and Piezoelectric-Induced Charge Separation and Molecular Oxygen Activation

Hongwei Huang, Shuchen Tu, Chao Zeng, Tierui Zhang, Ali H. Reshak, and Yihe Zhang**

Abstract: *Efficient photo- and piezoelectric-induced molecular oxygen activation are both achieved by macroscopic polarization enhancement on a noncentrosymmetric piezoelectric semiconductor $BiOIO_3$. The replacement of V^{5+} ions for I^{5+} in IO_3 polyhedra gives rise to strengthened macroscopic polarization of $BiOIO_3$, which facilitates the charge separation in the photocatalytic and piezoelectric catalytic process, and renders largely promoted photo- and piezoelectric induced reactive oxygen species (ROS) evolution, such as superoxide radicals ($\cdot O_2^-$) and hydroxyl radicals ($\cdot OH$). This work advances piezoelectricity as a new route to efficient ROS generation, and also discloses macroscopic polarization engineering on improvement of multi-responsive catalysis.*

Reactive oxygen species (ROS), such as superoxide ($\cdot O_2^-$), hydroxyl ($\cdot OH$), singlet oxygen ($^1O_2$), peroxyl ($RO_2\cdot$), and alkoxyl (RO-) as well as hypochlorous acid (HOCl), as highly-active and green oxidants, are of great significance for environmental chemistry and biochemistry.[1] Currently, the ROS are basically produced in photocatalytic process. For example, the photogenerated electron can reduce O_2 to $\cdot O_2^-$, and $\cdot OH$ are created via a hole oxidative process on H_2O and/or OH^-.[2] In particular, $\cdot OH$ is the most powerful and nonselective oxidant, and it can damage all types of organic/biomolecules.[3] As the fast carrier recombination (several ps) occurred in photocatalytic process, ROS evolution efficiency through photocatalysis is limited.[4] Recently, pyroelectrically driven $\cdot OH$ generation was achieved by synergism of ferroelectric $BaTiO_3$ and superficial Pd nanoparticles, but its efficiency is still low.[5] Thus, promoting photocatalytic ROS evolution as well as exploration of new channels to production of ROS, particularly realized by a single material, are of significance and challenge. Piezoelectrics reversibly converting stress into electricity, are widely applied in optoelectronics. The stress-induced polarization potential can act as alternating built-in electric field to separate photoinduced carriers.[6] $BiOIO_3$ as a noncentrosymmetric (NCS) polar material presents strong second-harmonic generation (SHG, ca. 12.5 KDP) and piezoelectricity ($d_{33} \approx 26\ pm\ V^{-1}$).[7] The large macroscopic polarity is mainly attributed to the alignment of the lone-pair-containing IO_3 polyhedra. Recently, $BiOIO_3$ was investigated for diverse photocatalytic applications.[8] Fan et al. and our group demonstrated that large macroscopic polarity can induce efficient charge separation, contributing to high photocatalytic activity.[9] Considering the large polarity of $BiOIO_3$ from IO_3 polyhedra, decoration on IO_3 may adjust the polarity, and thus improve photocatalytic molecular oxygen activation. Importantly, $BiOIO_3$ is piezoelectric. It is worth surveying its performance for piezoelectric-catalytic ROS generation.

Herein, we describe the synthesis and photo- and piezoelectric-induced molecular oxygen activation of vanadium-doped $BiOIO_3$. V is selected for replacing I in $BiOIO_3$ for the following two reasons: The similar bond length of V–O and I–O (ca. 1.6–1.9 Å) allows the replacement of V for I. Besides, the equivalent substitution of I^{5+} with V^{5+} can keep the charge conservation in $BiOIO_3$. The results revealed that V replacement could give rise to a large macroscopic polarization enhancement of $BiOIO_3$. It significantly promotes the charge separation in both the photocatalytic and piezoelectric catalysis process, which renders strengthened photo- and piezoelectric-induced molecular oxygen activation for producing $\cdot O_2^-$ and $\cdot OH$.

XRD demonstrates that V-$BiOIO_3$ keeps both the phase and crystallization orientation unchanged (Supporting Information, Figure S1). XPS was conducted to reveal the V doping. It is evident that a new peak at 529.9 eV appears for V-$BiOIO_3$, which is attributed to V 2p (Figure 1 a). The peaks at 530.4, 164.4, 159.1, 635.4, and 623.8 eV observed for $BiOIO_3$ correspond well to O 1s, Bi $4f_{5/2}$, Bi $4f_{7/2}$, I $3d_{3/2}$, and I $3d_{5/2}$, respectively (Supporting Information, Figure S2). In contrast, the above peaks of V-$BiOIO_3$ all show a distinct shift, which means the chemical environment change of related atoms. From Raman spectra (Figure 1 b), an obvious band can be seen around 850 cm^{-1} for V-$BiOIO_3$, which can be ascribed to the V–O vibration.[10]

To deeply understand the crystal structural evolution and the V action in the $BiOIO_3$ structure, Rietveld refinement was carried out via the computer software General Structure Analysis System (GSAS). The result show that V-$BiOIO_3$ also crystallizes in orthorhombic $Pca2_1$ space group, and I^{5+} and V^{5+} ions with ratio of 0.925(3)/0.074(7) co-occupy in the same

[*] Dr. H. W. Huang, S. C. Tu, C. Zeng, Prof. Y. H. Zhang
Beijing Key Laboratory of Materials Utilization of Nonmetallic Minerals and Solid Wastes, School of Materials Science and Technology, China University of Geosciences, Beijing 100083 (China)
E-mail: hhw@cugb.edu.cn
zyh@cugb.edu.cn
Prof. T. R. Zhang
Key Laboratory of Photochemical Conversion and Optoelectronic Materials, Technical Institute of Physics and Chemistry
Chinese Academy of Sciences, Beijing 100190 (China)
Prof. A. H. Reshak
New Technologies—Research Centre, University of West Bohemia
Univerzitni 8, 306 14 Pilsen (Czech Republic)
Supporting information and the ORCID identification number(s) for the author(s) of this article can be found under: https://doi.org/10.1002/anie.201706549.

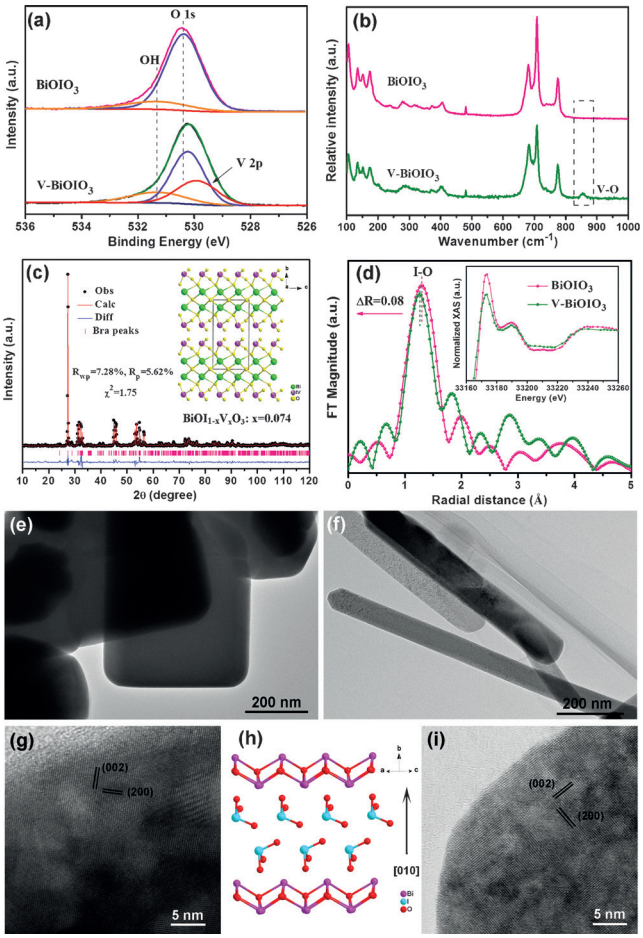

Figure 1. a) XPS of O 1s and V 2p and b) Raman spectra of $BiOIO_3$ and V-$BiOIO_3$ ($BiOI_{0.926}V_{0.074}O_3$). c) XRD Rietveld refinement of V-$BiOIO_3$. d) Fourier-transform (FT) curves of XAFS data of $BiOIO_3$ and V-$BiOIO_3$. e)–i) TEM images of e),g) $BiOIO_3$ and f),i) V-$BiOIO_3$. h) Unit cell illustration of $BiOIO_3$.

site (Figure 1c). Namely, the final V-$BiOIO_3$ is $BiI_{1-x}V_xO_4$: $x = 0.074(7)$. The corresponding crystallographic data are summarized in the Supporting Information, Tables S1–S3. The unit cell parameters undergo slight changes resulting from the substitution of I^{5+} with V^{5+} according to Vegard's rule. For confirmation, XAFS data on the I K-edge (33.179 keV) of pristine $BiOIO_3$ and $BiOI_{0.926}V_{0.074}O_3$ were collected at room temperature. The Bi L-edge oscillation curves of $BiOIO_3$ and $BiOI_{0.926}V_{0.074}O_3$ display obvious difference in the energy range of 33160–33260 eV, which suggests their different local atomic arrangements (inset of Figure 1d). Figure 1d presents the Fourier transform (FT) curves of XAFS data. The strong peak between 1 and 2 Å is attributed to I–O bond. Remarkably, the I–O radial distance shows an evident shift (0.08 Å) to smaller value, which is resulted from the replacement of V^{5+} for I^{5+}. It is in accordance with the fact that V–O has a slightly shorter bond length than I–O. The replacement of V^{5+} would induce a distortion of IO_3 polyhedron.

SEM and TEM revealed that the morphology of $BiOIO_3$ undergoes great change after V replacement. The original 2D square nanoplates transform into 1D nanostrips (Figure 1e,f; Supporting Information, Figure S3a–d). HRTEM showed that the interplanar spacing of lattice fringe for $BiOIO_3$ and $BiOI_{0.926}V_{0.074}O_3$ is about 0.287 nm, corresponding to (002) and (200) planes. Their FFT patterns are also well assigned to the [010] zone-axis diffraction spots of orthorhombic $BiOIO_3$ or $BiOI_{0.926}V_{0.074}O_3$ (Supporting Information, Figure S3e,f). Namely, the exposing facet for both samples is the {010} facet (Figure 1g,i). It is perpendicular to the $[Bi_2O_2]^{2+}$ layer stacking direction (Figure 1h), where the internal electric field favors charge separation. Besides, the specific surface area of $BiOIO_3$ and $BiOI_{0.926}V_{0.074}O_3$ is determined to be 3.1 and 8.7 $m^2 g^{-1}$, respectively, fitting the nonporous characteristic (Supporting Information, Figure S4). Namely, the V replacement in $BiOIO_3$ causes a 2.5-fold increase in surface area.

Diffuse reflectance spectra reveal that $BiOI_{0.926}V_{0.074}O_3$ shows visible light absorption with a long absorption tail extending to 550 nm compared with $BiOIO_3$ (Supporting Information, Figure S5), corresponding to the color change from white to yellow. This would allow $BiOIO_3$ visible-light-active photoreactivity. The band gap was determined as 3.07 and 2.95 eV for $BiOIO_3$ and $BiOI_{0.926}V_{0.074}O_3$, respectively (Supporting Information, Figure S7a). DFT calculations[11] demonstrated that the narrowed band gap and visible-light absorption of $BiOI_{0.926}V_{0.074}O_3$ are mainly resulted by the downshift of conduction band (Supporting Information, Figures S6a and Figure S7b), which is contributed by the V 3d orbital (Supporting Information, Figure S6c–e).

Photoinduced molecular oxygen activation was studied under visible light ($\lambda > 420$ nm) and UV light. DMPO-assisted ESR inspects the spin-trapped paramagnetic oxygen species $^{\bullet}O_2^-$ and $^{\bullet}OH$.[2c] $BiOIO_3$ shows no signal under visible light, confirming no visible-light activity of $BiOIO_3$ (Figure 2a,b). Whereas, evident six identical peaks are observed for $BiOI_{0.926}V_{0.074}O_3$, which is assigned to DMPO-$^{\bullet}O_2^-$ adduct derived from O_2 reduction by electrons.[12] Meanwhile, four

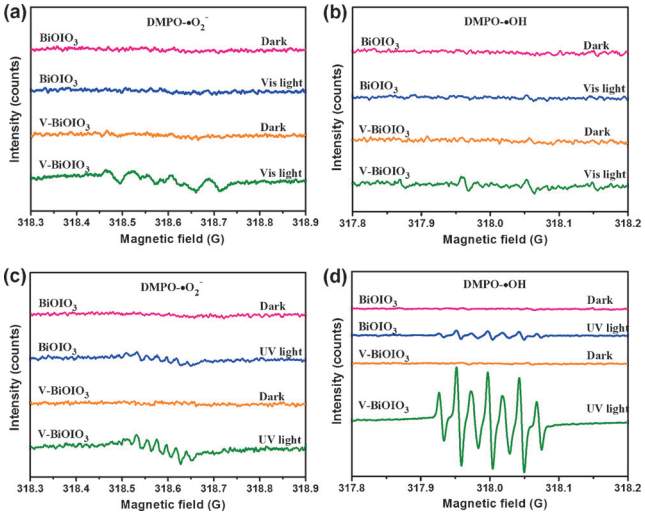

Figure 2. ESR signals for a),c) DMPO-$^{\bullet}O_2^-$ and b),d) DMPO-$^{\bullet}OH$ over $BiOIO_3$ and V-$BiOIO_3$ ($BiOI_{0.926}V_{0.074}O_3$) under visible-light ($\lambda > 420$ nm) and UV light illumination, respectively, for 5 min.

peaks with intensities of 1:2:2:1 attributing to DMPO-·OH also appear.[2c] ·OH should originate from the OH^-/H_2O oxidation in water by holes. It demonstrates that V replacement endows $BiOIO_3$ with the visible-light molecular oxygen activation ability with generation of the above two powerful oxidative species. This is understandable because $BiOI_{0.926}V_{0.074}O_3$ exhibit photoabsorption in visible region. However, it is significant to find that this property is also greatly enhanced with irradiation of UV light. $BiOI_{0.926}V_{0.074}O_3$ shows a stronger six-line spectrum than $BiOIO_3$ under UV light (Figure 2c,), meaning a higher $\cdot O_2^-$ production. Remarkably, a significantly strengthened seven-line spectrum was generated by $BiOI_{0.926}V_{0.074}O_3$ (Figure 2d). This type of peaks with intensity of 1:2:1:2:1:2:1 represents the appearance of DMPOX, resulting from the oxidation of DMPO by two ·OH radicals.[13] As the amount of free radical is approximately proportional to the square of the height of signal,[14] the $\cdot O_2^-$ and ·OH amounts for $BiOI_{0.926}V_{0.074}O_3$ is calculated to be about 3.5 and 95.5 times that of $BiOIO_3$. This observation clearly states that a more powerful UV-light-driven ROS evolution ability was achieved for $BiOI_{0.926}V_{0.074}O_3$ than the pristine $BiOIO_3$ compared to visible-light-activity enhancement, and the enormously intensified activity is not associated with photoabsorption.

To further understand the drastically promoted ROS activity, photodegradation on a dye model RhB was performed (Supporting Information, Figures S8–S11). The photocatalytic activity of $BiOI_{0.926}V_{0.074}O_3$ is about 10.1 and 21.1 times that of $BiOIO_3$ under visible and UV light, respectively (Figure 3a,b). An active species trapping test shows that $\cdot O_2^-$ and ·OH are the main reactive species and take crucial roles in the photocatalytic oxidation reaction regardless of light source (Supporting Information, Figures S12 and S13).[15] These results well confirmed the highly enhanced molecular oxygen activation of $BiOI_{0.926}V_{0.074}O_3$.

For exploring the origin for the enormously enhanced photoreactivity, several factors that predominantly affect the photochemical reaction, for example, photoabsorption, surface area, and charge separation efficiency are considered. As revealed by the above data, the extended photoabsorption in visible region of $BiOI_{0.926}V_{0.074}O_3$ is not responsible for the improved UV-light activity. Their surface area difference (ca. 2.5 times) is also far small to contribute to huge enhancement on ROS generation and photodegradation. Therefore, charge separation as the most possible factor is investigated by transient photocurrent and SPV spectroscopy.[16] $BiOI_{0.926}V_{0.074}O_3$ produces a markedly increased current density under UV light (Figure 3c), beyond 5 times that of $BiOIO_3$, indicating a higher charge separation in $BiOI_{0.926}V_{0.074}O_3$. SPV spectroscopy can reveal the surface potential barrier and charge separation extent of excited states generated by absorption. It is demonstrated that the SPV signal generated by $BiOI_{0.926}V_{0.074}O_3$ far exceeds that of $BiOIO_3$ in the range of 310–390 nm, with enhancement degree of over 10-fold (Figure 3d). These results illuminates that the V replacement endues $BiOIO_3$ with significantly promoted charge separation, accounting for the robust molecular oxygen activation performance. In view of that $BiOI_{0.926}V_{0.074}O_3$ and $BiOIO_3$ have the same exposing {010} facet, there must exist some other reasons for the dramatically strengthened charge separation.

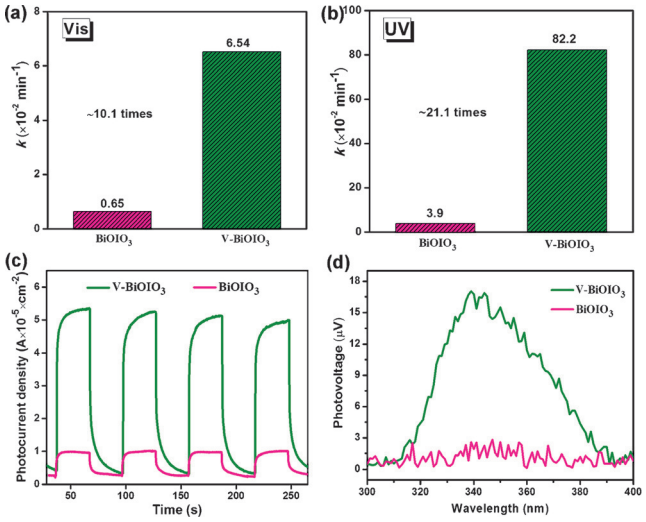

Figure 3. Reaction-rate constant for RhB degradation over $BiOIO_3$ and V-$BiOIO_3$ ($BiOI_{0.926}V_{0.074}O_3$) under a) visible light ($\lambda > 420$ nm) and b) UV light. c) Transient photocurrent response and d) surface photovoltage spectra over $BiOIO_3$ and V-$BiOIO_3$ under UV light.

Polarization induced in the NCS crystal structure can cause a large intrinsic polarization effect, promoting charge separation.[9] The polarity of $BiOIO_3$ mainly originates from alignment of IO_3 polyhedra along [001] direction. Along the *a* and *b* axis, the polarity of IO_3 polyhedra is offset due to the completely opposite arrangement of IO_3 groups (Figure 4a), while along the c-axis, namely [001] direction, the local dipole moment of IO_3 polyhedra is additive, which results in a large macroscopic polarization (Figure 4b).[7] As revealed by TEM, $BiOI_{0.926}V_{0.074}O_3$ crystal grows along the [001] direction. This crystallization orientation may be induced by the polarization. SHG performed by irradiation of a 1064 nm Nd:YAG laser confirms the enhanced macroscopic polarity in $BiOI_{0.926}V_{0.074}O_3$, which produces a superior SHG response, beyond two times that of $BiOIO_3$ (Figure 4c). It verifies that a larger macroscopic polarity is realized in $BiOI_{0.926}V_{0.074}O_3$, favorable for the separation of photogenerated electrons and holes.[9b] For in-depth understanding, the strengthened macroscopic polarization of $BiOI_{0.926}V_{0.074}O_3$ is analyzed by polyhedral distortion index. The symmetry of coordination environment in crystal structure can be influenced by the polyhedral distortion. The polyhedral distortion index *D* can be calculated by Equation (1)[17]

$$D = \frac{1}{n}\sum_{i=1}^{n}\frac{|l_i - l_{av}|}{l_{av}} \quad (1)$$

where l_i is the distance from the central atom to the *i*th ligands and l_{av} is the average bond length. The polyhedral distortion of IO_3 is determined to be 0.065 in $BiOI_{1-x}V_xO_3$:$x = 0.074(7)$, which is bigger than that of $BiOIO_3$ (0.063). Therefore, the superimposition of microscopic polyhedral distortion contributes to the large macroscopic polarization of $BiOI_{0.926}V_{0.074}O_3$.

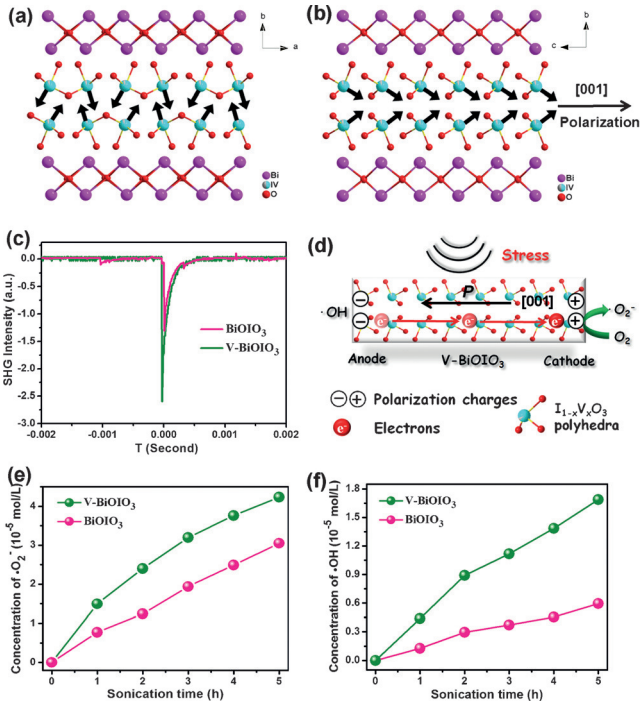

Figure 4. Crystal structure of V-$BiOIO_3$ ($BiOI_{0.926}V_{0.074}O_3$) a) along *a–b* and b) along *b–c* planes (Black arrows indicate polarization direction of $I_{1-x}V_xO_3$). c) SHG generation for $BiOIO_3$ and $BiOI_{0.926}V_{0.074}O_3$. e) $\cdot O_2^-$ and f) ·OH evolution curves over $BiOIO_3$ and $BiOI_{0.926}V_{0.074}O_3$ under ultrasonic irradiation (40 kHz, 300 W).

As $BiOIO_3$ is piezoelectric, polarization enhancement caused by V replacement may also result in an improved piezoelectric-induced molecular oxygen activation ability. Here, ultrasonic agitation was employed as a stable irradiation source to provide stress, and NBT was used as a probe to quantify the $\cdot O_2^-$ concentration.[18] Sharp decrease in the absorbance of NBT centering at 259 nm is observed, demonstrating that both $BiOIO_3$ and $BiOI_{0.926}V_{0.074}O_3$ show robust pizeoelectric-catalytic activity for transforming O_2 into $\cdot O_2^-$ (Supporting Information, Figure S14). Based on the reacting relation between NBT and $\cdot O_2^-$ (1:4 in molar ratio),[18] the average $\cdot O_2^-$ evolution rate of $BiOIO_3$ and $BiOI_{0.926}V_{0.074}O_3$ is determined to be 6.5 and 11.1 $\mu mol\,L^{-1}\,h^{-1}$, respectively (Figure 4e). To inspect if ·OH was generated in the piezoelectric-induced process, terephthalic acid (TA)-photoluminescence (PL) method is employed, as ·OH could react with TA in equal proportion to produce highly fluorescent 2-hydroxyterephthalic acid at 425 nm.[5] Drastic PL peak intensity increase occurs with increasing the ultrasonic time (Supporting Information, Figure S15), suggesting the continuous production of ·OH. The plot of ·OH concentration vs. ultrasonic irradiation time is illustrated in Figure 4f. The ·OH concentration generated by $BiOI_{0.926}V_{0.074}O_3$ far exceeds that by $BiOIO_3$, and the average production rates are 1.2 and 3.9 $\mu mol\,L^{-1}\,h^{-1}$ for $BiOIO_3$ or $BiOI_{0.926}V_{0.074}O_3$, respectively. Therefore, $BiOI_{0.926}V_{0.074}O_3$ shows a much superior pizeoelectric-induced $\cdot O_2^-$ and ·OH evolution, approximately 1.7 and 3.3 times of $BiOIO_3$. Besides, no $\cdot O_2^-$ and ·OH are detected under ultrasonic agitation without $BiOIO_3$ or $BiOI_{0.926}V_{0.074}O_3$ (Supporting Information, Figure S16), further verifying the piezoelectric induced ROS evolution process.

On the basis of the above results, the possible piezoelectric-catalytic molecular oxygen activation and enhancement mechanism is speculated. As $BiOIO_3$ is pizeoelectric, the ultrasonic-introduced press could induce the generation and asymmetrical distribution of positive and negative charges on two opposite sides of $BiOIO_3$. According to the metal oxide anode radical production theory, the electrocatalytic effect would occur, which is induced by the as-generated electric charges [Equations (2) and (3)]:[19]

$$BiOIO_3 + H_2O \rightarrow BiOIO_3 + \cdot OH + H^+ + e^- \quad (2)$$

$$O_2 + e^- \rightarrow \cdot O_2^- \quad (3)$$

During the electrocatalytic process, ·OH, H^+, and e^- were generated at the anode. As the anode of $BiOIO_3$ nanostrips bears ultrasonic-induced polarization negative charges, and cathode is positively charged, the piezoelectric polarization field goes from cathode to anode. Owing to charge interaction, the e^- produced at anode would migrate to cathode, and reduce O_2 into $\cdot O_2^-$. In view of the much stronger polarity of $BiOI_{0.926}V_{0.074}O_3$ than $BiOIO_3$ along the [001] direction, higher charge separation occurs for $BiOI_{0.926}V_{0.074}O_3$. Therefore, more $\cdot O_2^-$ and ·OH are produced from $BiOI_{0.926}V_{0.074}O_3$. Besides, the nanostrip morphology of $BiOI_{0.926}V_{0.074}O_3$ strengthens the asymmetrical distribution of positive and negative charges on its surface, further contributing to the ROS production.

In summary, both photo- and piezoelectric-induced molecular oxygen activation are achieved on a NCS piezoelectric $BiOIO_3$. More fascinatingly, the replacement of V^{5+} for I^{5+} ions in IO_3 polyhedra resulted in a macroscopic polarization enhancement, which largely facilitates the charge separation, and thus resulting in highly promoted molecular oxygen activation in both the photocatalytic and ultrasonic-assisted piezoelectric-catalytic process. Compared to pure $BiOIO_3$, the $\cdot O_2^-$ and ·OH evolution rates for $BiOI_{0.926}V_{0.074}O_3$ increase separately about 3.5 and 95.5 fold for photocatalysis, and 1.7 and 3.3 times for piezoelectric-catalysis. Besides, the formation mechanism of reactive oxygen species in piezoelectric-catalytic process was speculated. This study exposes the promising prospect of macroscopic polarization enhancement on promoting photo/piezoelectric catalysis, and may have potentials to be extended to other applications, such as supercapacitors and lithium-ion batteries.

Acknowledgements

This work was supported by the National Natural Science Foundations of China (Grant No. 51672258 and 51572246), the Fundamental Research Funds for the Central Universities (2652015296), CENTEM project CZ.1.05/2.1.00/03.0088.

Conflict of interest

The authors declare no conflict of interest.

Keywords: $BiOIO_3$ · macroscopic polarization · molecular oxygen activation · photocatalysis · piezoelectric catalysis

How to cite: *Angew. Chem. Int. Ed.* **2017**, *56*, 11860–11864
Angew. Chem. **2017**, *129*, 12022–12026

[1] a) A. L. Linsebigler, G. Q. Lu, J. T. Yates, *Chem. Rev.* **1995**, *95*, 735; b) Y. Li, W. Zhang, J. F. Niu, Y. S. Chen, *ACS Nano* **2012**, *6*, 5164; c) M. A. Henderson, I. Lyubinetsky, *Chem. Rev.* **2013**, *113*, 4428.

[2] a) K. Zhao, L. Z. Zhang, J. J. Wang, Q. X. Li, W. W. He, J. J. Yin, *J. Am. Chem. Soc.* **2013**, *135*, 15750; b) Y. B. Zhao, W. H. Ma, Y. Li, H. W. Ji, C. C. Chen, H. Y. Zhu, J. C. Zhao, *Angew. Chem. Int. Ed.* **2012**, *51*, 3188; *Angew. Chem.* **2012**, *124*, 3242; c) H. W. Huang, X. W. Li, J. J. Wang, F. Dong, P. K. Chu, T. R. Zhang, Y. H. Zhang, *ACS Catal.* **2015**, *5*, 4094.

[3] L. Brunet, D. Y. Lyon, E. M. Hotze, P. J. J. Alvarez, M. R. Wiesner, *Environ. Sci. Technol.* **2009**, *43*, 4355.

[4] J. Li, L. J. Cai, J. Shang, Y. Yu, L. Z. Zhang, *Adv. Mater.* **2016**, *28*, 4059.

[5] A. Benke, E. Mehner, M. Rosenkranz, E. Dmitrieva, T. Leisegang, H. Stöcker, W. Pompe, D. C. Meyer, *J. Phys. Chem. C* **2015**, *119*, 18278.

[6] H. D. Li, Y. H. Sang, S. J. Chang, X. Huang, Y. Zhang, R. S. Yang, H. D. Jiang, H. Liu, Z. L. Wang, *Nano Lett.* **2015**, *15*, 2372.

[7] S. D. Nguyen, J. Yeon, S. H. Kim, P. S. Halasyamani, *J. Am. Chem. Soc.* **2011**, *133*, 12422.

[8] a) W. J. Wang, B. B. Huang, X. C. Ma, Z. Y. Wang, X. Y. Qin, X. Y. Zhang, Y. M. Dai, H. Whangbo, *Chem. Eur. J.* **2013**, *19*, 14777; b) H. W. Huang, H. Ye, R. He, X. X. Jiang, Z. S. Lin, Y. H. Zhang, S. C. Wang, *Inorg. Chem. Commun.* **2014**, *40*, 215; c) X. M. Qi, M. L. Gu, X. Y. Zhu, J. Wu, H. M. Long, K. He, Q. Wu, *Chem. Eng. J.* **2016**, *285*, 11; d) Y. Su, L. Zhang, W. Z. Wang, *Int. J. Hydrogen Energy* **2016**, *41*, 10170.

[9] a) X. Y. Fan, L. Zang, M. Zhang, H. S. Qiu, Z. Wang, J. Yin, H. Z. Jia, S. L. Pan, C. Y. Wang, *Chem. Mater.* **2014**, *26*, 3169; b) H. W. Huang, Y. He, X. W. Li, M. Li, C. Zeng, F. Dong, X. Du, T. R. Zhang, Y. H. Zhang, *J. Mater. Chem. A* **2015**, *3*, 24547.

[10] K. H. Ye, Z. S. Chai, J. W. Gu, X. Yu, C. X. Zhao, Y. M. Zhang, W. J. Mai, *Nano Energy* **2015**, *18*, 222.

[11] a) M. C. Payne, M. P. Teter, D. C. Allan, T. A. Arias, J. D. Joannopoulos, *Rev. Mod. Phys.* **1992**, *64*, 1045; b) Z. Y. Sun, L. Zhang, F. Dang, Y. Liu, Z. Y. Fei, Q. Shao, H. Lin, J. Guo, L. C. Xiang, N. Yerra, Z. H. Guo, *CrystEngComm* **2017**, *19*, 3288.

[12] S. X. Weng, Z. X. Pei, Z. Y. Zheng, J. Hu, P. Liu, *ACS Appl. Mater. Interfaces* **2013**, *5*, 12380.

[13] G. M. Rosen, E. J. Rauckman, *Mol. Pharmacol.* **1980**, *17*, 233.

[14] Y. X. Li, S. X. Ouyang, H. Xu, X. Wang, Y. P. Bi, Y. F. Zhang, J. H. Ye, *J. Am. Chem. Soc.* **2016**, *138*, 13289–13297.

[15] H. W. Huang, X. Han, X. W. Li, S. C. Wang, P. K. Chu, Y. H. Zhang, *ACS Appl. Mater. Interfaces* **2015**, *7*, 482.

[16] H. Y. Zhu, X. Chen, Z. F. Zheng, X. B. Ke, E. Jaatinen, J. C. Zhao, C. Guo, T. F. Xie, D. J. Wang, *Chem. Commun.* **2009**, 7524–7526.

[17] K. A. Denault, J. Brgoch, M. W. Gaultois, A. Mikhailovsky, R. Petry, H. Winkler, S. P. DenBaars, R. Seshadri, *Chem. Mater.* **2014**, *26*, 2275–2282.

[18] L. Q. Ye, K. J. Deng, F. Xu, L. H. Tian, T. Y. Peng, L. Zan, *Phys. Chem. Chem. Phys.* **2012**, *14*, 82–85.

[19] C. Comninellis, *Electrochim. Acta* **1994**, *39*, 1857–1862.

Manuscript received: June 29, 2017
Accepted manuscript online: July 21, 2017
Version of record online: August 16, 2017

